Structural variability of EspG chaperones from mycobacterial ESX-1, ESX-3 and ESX-5 type VII secretion systems

Anne T. Tuukkanen[1], Diana Freire[1], Sum Chan[2], Mark A. Arbing[2], Robert W. Reed[3#], Timothy J. Evans[3#], Grasilda Zenkeviciutė[1&], Jennifer Kim[2], Sara Kahng[2], Michael R. Sawaya[2], Matthias Wilmanns[1], David Eisenberg[2], Annabel H. A. Parret[1*], Konstantin V. Korotkov[3*]

[1] European Molecular Biology Laboratory, Hamburg Unit, Hamburg, 22607, Germany

[2] UCLA-DOE Institute, University of California Los Angeles, Los Angeles, California, 90095, United States of America

[3] Department of Molecular & Cellular Biochemistry, and Center for Structural Biology, University of Kentucky, Lexington, Kentucky, 40536, United States of America

[#] Present address: Division of Regulatory Services, College of Agriculture, Food and Environment, University of Kentucky, Lexington, Kentucky, 40536, United States of America

[&] Present address: Department of Pharmacology, University of Cambridge, Cambridge, CB2 1PD, United Kingdom

* Correspondence to: Annabel H. A. Parret (parret@embl-hamburg.de), Konstantin V. Korotkov (kkorotkov@uky.edu)

Abstract

Type VII secretion systems (ESX) are responsible for transport of multiple proteins in mycobacteria. How different ESX systems achieve specific secretion of cognate substrates remains elusive. In the ESX systems, the cytoplasmic chaperone EspG forms complexes with heterodimeric PE-PPE substrates that are secreted from the cells or remain associated with the cell surface. Here we report the crystal structure of the $EspG_1$ chaperone from the ESX-1 system determined using a fusion strategy with T4 lysozyme. $EspG_1$ adopts a quasi 2-fold symmetric structure that consists of a central β-sheet and two α-helical bundles. Additionally, we describe the structures of $EspG_3$ chaperones from four different crystal forms. Comparison of available $EspG_3$ structures reveals several conformations of the putative PE-PPE binding site. Analysis of $EspG_1$, $EspG_3$ and $EspG_5$ chaperones using small-angle X-ray scattering (SAXS) reveals that $EspG_1$ and $EspG_3$ chaperones form dimers in solution, which we observed in several of our crystal forms. Finally, we propose a model of the ESX-3 specific PE5-PPE4-$EspG_3$ complex based on the SAXS analysis.

Highlights

- The crystal structure of $EspG_1$ reveals the common architecture of the type VII secretion system chaperones
- Structures of $EspG_3$ chaperones display a number of conformations that could reflect alternative substrate binding modes
- $EspG_3$ chaperones dimerize in solution
- A model of $EspG_3$ in complex with its substrate PE-PPE dimer is proposed based on SAXS data

Abbreviations used:

EOM, ensemble optimization method; MD, molecular dynamics; rmsd, root-mean-square deviation; NSD, normalized spatial discrepancy; RMSF, Root-Mean-Square-Fluctuations; SAXS, small angle X-ray scattering; SEC, size-exclusion chromatography; SeMet, selenomethionine; TEV, tobacco etch virus; TCEP, tris(2-carboxyethyl)phosphine

Keywords: *Mycobacterium tuberculosis* / protein export / small-angle X-ray scattering / PE-PPE proteins

Introduction

The most deadly bacterial pathogen worldwide is *Mycobacterium tuberculosis* (*Mtb*), which causes tuberculosis (TB). While many infectious diseases can be controlled by vaccination, TB lacks an effective vaccine and even prior infection with *Mtb* does not provide lasting immunity. Moreover, standard anti-TB therapy requires the use of a combination of drugs for six months, which leads to poor compliance and to emergence of drug resistance [1]. Even more threatening is the global increase in extensively drug-resistant *Mtb* and the emergence of extremely drug-resistant *Mtb*. Anti-virulence drugs targeting mycobacterial secretion have the potential to become a valuable alternative to classical antibiotics [2]. During infection, pathogenic mycobacteria use several related protein secretion pathways designated ESX systems [3-5]. The *Mtb* genome encodes five such secretion systems, ESX-1 through ESX-5. Each consists of ATPases, membrane proteins, a protease, accessory proteins, and secreted substrates [6, 7]. Four conserved components of the ESX-5 system — $EccB_5$, $EccC_5$, $EccD_5$ and $EccE_5$ — form a platform complex with six-fold symmetry that is embedded in the mycobacterial inner membrane [8, 9]. The ESX-1 core complex is composed of paralogous components [10], which suggests that all ESX systems assemble into similar complexes. Many ESX-secreted substrates are interdependent on each other for secretion, suggesting that they might be a part of the ESX secretion machinery [11, 12]. The most abundant class of ESX substrates is represented by the so-called PE and PPE proteins [13]. These proteins generally form alpha-helical heterodimers that are probably secreted in a folded conformation [14]. Several PE/PPE proteins are major antigens for TB diagnostic and vaccine development [15-19]. Importantly, PE/PPE proteins are secreted specifically by only one of the five ESX secretion systems [20-24] raising the question of how various ESX systems discriminate among PE/PPE substrates.

Previously it was demonstrated that PE/PPE protein secretion in *Mycobacterium marinum* is impaired upon disruption of the *espG* gene encoded within its respective ESX gene locus leading to accumulation of substrates in the bacterial cytosol [25]. The crystal structure of the heterotrimeric PE25–PPE41–$EspG_5$ protein complex revealed that $EspG_5$

interacts with a PE25–PPE41 heterodimer by binding to a hydrophobic patch at the tip of PPE41 [26, 27]. The general YxxD/E secretion motif [28, 29] at the distal end of PE25 is free to interact with the ESX-5 secretion machinery in the inner membrane, probably by interaction with the Ftsk/SpoIIIE-like ATPase $EccC_5$ [30, 31]. In addition, $EspG_5$ was reported to improve solubility of aggregation-prone PE–PPE pairs upon co-expression [26, 32]. Thus, EspG acts as a disaggregase of ESX substrates in the cytosol prior to secretion. Moreover, substrate specificity is determined by the EspG-binding domain of PPE proteins as demonstrated by substrate re-routing experiments [33]. While structures of the $EspG_5$ chaperone in complexes with PE–PPE substrates and a monomeric $EspG_3$ chaperone have been reported [26, 27, 34], structural information on $EspG_1$ is lacking.

In this study, we report the first crystal structure of an $EspG_1$ chaperone from *Mycobacterium kansasii* and four crystal structures of $EspG_3$ from *M. smegmatis and M. marinum*. We analyze here the available atomic structures of EspG chaperones and present a thorough study of the conformational variability of EspG proteins in apo and substrate-bound forms (PE–PPE–EspG) using small-angle X-ray scattering (SAXS). In addition, we characterize the SAXS-based rigid-body structure of the PE5–PPE4–$EspG_3$ protein complex in solution and compare it to the atomic structure of PE25–PPE41–$EspG_5$ in order to obtain further insights into protein flexibility and substrate recognition. Our study suggests that the EspG chaperones are capable of adopting multiple conformational states, likely a key determinant of their ability to recognize multiple PE–PPE substrates.

Results

The crystal structure of *M. kansasii* $EspG_1$

Initial attempts to crystallize *M. tuberculosis* $EspG_1$ ($EspG_{1mtu}$) were not successful; therefore we screened several homologs of $EspG_1$ from other mycobacterial species. We obtained microcrystals using an optimized construct of *M. kansassi* $EspG_1$ ($EspG_{1mka}$) that has 80% sequence identity with $EspG_{1mtu}$ (see Methods) (Supplementary Fig. S1). However,

extensive optimization of these crystals did not lead to diffraction quality crystals. To overcome these difficulties, we utilized a fusion approach using T4 lysozyme (T4L) as an N-terminal fusion. Crystals of the T4L-$EspG_{1mka}$ fusion could be readily optimized and diffracted to 2.27 Å resolution. The structure of T4L-$EspG_{1mka}$ was solved by molecular replacement and refined to R_{work} 0.214 and R_{free} 0.251 with good geometry (Table 1). The structure contains two molecules in the asymmetric unit (Fig. 1a) with an extensive interface between the T4L moieties (2250 $Å^2$ buried surface area). Surprisingly, part of the TEV cleavage sequence at the N-terminus of T4L is ordered in the structure and contributes both to the T4L dimer interface (849 $Å^2$ buried surface area corresponding to 38% of the T4L–T4L interface) and the intra-subunit contacts between T4L and $EspG_{1mka}$. The conformations of the two copies of $EspG_{1mka}$ in the asymmetric unit are very similar and superimpose with a root-mean-square deviation (rmsd) of 1.0 Å over 231 Cα atoms (Supplementary Fig. S2a). $EspG_{1mka}$ has a typical EspG fold characterized by a central anti-parallel β-sheet and two α-helical bundles (Fig. 1b). The N-terminal and C-terminal subdomains of $EspG_{1mka}$ are related by a quasi two-fold symmetry, have 10% sequence identity, and can be superimposed with a rmsd of 2.7 Å over 71 Cα atoms (Supplementary Fig. S3). Several parts of the $EspG_{1mka}$ structure did not have interpretable electron density and were not modeled, including the loop preceding the α2 helix (chains A and B), the β2–β3 loop (chain A), part of the β6 strand (chain B), and the α6 helix (chains A and B). The residues corresponding to the C-terminal helical bundle displayed higher *B* factors compared to other parts of the structure (Supplementary Fig. S2b). The C-terminal helical bundle likely forms part of the substrate recognition site and could become more ordered upon binding of a cognate PE–PPE dimer.

The EspG fold is conserved in ESX-1, ESX-3 and ESX-5 systems

In order to extend structural knowledge on this interaction and the differences between EspG-substrate interactions from ESX-1, ESX-3 and ESX-5 secretion systems, we determined additional crystal structures of the EspG chaperones from the ESX-1 and ESX-3

systems (Table 1). Despite the fact that EspG chaperones display the lowest level of protein sequence similarity (13–23% sequence identity) of all the core components of the ESX systems, the $EspG_1$, $EspG_3$ and $EspG_5$ structures have a highly similar fold (Fig. 2, Fig. 3, Supplementary Figs. S4 and S5 and Supplementary Table S1). Rmsd of the aligned atoms for EspG superposition is 2.4 Å over 224 Cα atoms for $EspG_{1mka}$ vs. $EspG_{5mtu}$, 2.4 Å for $EspG_{3mma}$ vs. $EspG_{5mtu}$ over 238 Cα atoms and 2.4 Å for $EspG_{1mka}$ vs. $EspG_{3mma}$ over 234 Cα atoms. Despite the high overall structural similarity, the C-terminal helical bundles of $EspG_{1mka}$ and $EspG_3$ structures have a distinct conformation, when compared to $EspG_{5mtu}$ bound to the PE25–PPE41 dimer, which appears to be incompatible with substrate binding (Fig. 3). Another significant difference is the length and the conformation of the β2–β3 loop. In the PE25–PPE41–$EspG_{5mtu}$ structure (PDB ID 4KXR [26]), it extends 24 amino acid residues (Arg^{91}-Glu^{115}) and interacts strongly with the PE25–PPE41 dimer, whereas, for example, in the $EspG_{3msm}$ (PDB ID 4L4W) structure the loop consists of only 12 amino acid residues (Ser^{87}-Leu^{98}). These structural differences could be explained by conformational changes in $EspG_{5mtu}$ induced by PE–PPE binding, suggesting that binding of $EspG_1$ and $EspG_3$ to their cognate PPE protein partners is different from the PPE41–$EspG_5$ interaction observed in the PE25–PPE41–$EspG_5$ structure.

Variation of quaternary structure within EspG protein family

Analysis of crystal packing in the available $EspG_3$ structures revealed a number of possible quaternary arrangements in addition to the monomeric state. Firstly, a “wing-shaped dimer” was found in the asymmetric unit of the $EspG3_{msm}$ (PDB ID 4L4W) structure with 1892 $Å^2$ buried surface area (Fig. 4). The dimeric interface is mediated by residues from the C-terminal helical bundles and strands β6, β10, β11 and helix α8. In contrast, the asymmetric unit in $EspG_{3msm}$ (PDB ID 4RCL) structure contains a dimer in front-to-front orientation with 1761 $Å^2$ buried surface area. The β8 strands from the two subunits are located at the core of the interface and form an inter-subunit β-sheet. This dimeric conformation is further referred

to as a "β8-mediated dimer". However, in addition a "wing-shaped dimer" similar to the $EspG_{3msm}$ (PDB ID 4L4W) structure is present in the crystal lattice, with 2054 $Å^2$ buried surface area. Furthermore, the asymmetric unit of $EspG_{3msm}$ (PDB ID 4W4J [27]) structure also contains a similar wing-shaped dimer with substantial buried surface area as well as the β8-mediated dimer (Fig. 4).

Altogether, $EspG_3$ wing-shaped dimers are observed in three independent crystal structures, and β8-mediated dimers are seen in two crystal structures. The dimer interfaces are highly similar, with the subunits rotated relative to each other by 12 degrees in the wing-shaped dimers and 5 degrees in the β8-mediated dimers (Supplementary Fig. S6). The different quaternary structures of EspG chaperones reflect the variability that exists within this protein family (Table 2). As previously proposed [26], EspG likely acts as a chaperone that maintains PE/PPE secretion targets in the cytosol in a soluble state. To allow this, the PE–PPE interaction interface of EspG proteins must be available for effector binding. Superposition of the crystal structure of the PE25–PPE41–$EspG_5$ complex with the three different $EspG_3$ conformations observed in this study shows an accessible PE–PPE interaction interface in case of the EspG monomer and the wing-shaped dimer. In contrast, the β8-mediated $EspG_3$ conformation would be unable to bind secreted effectors given that the PE–PPE interaction interface of EspG is occluded (Supplementary Fig. S7). To assess whether EspG proteins of ESX-1 and ESX-5 display similar oligomerization behavior in solution, we performed a structural analysis of several EspG proteins in solution.

Concentration-dependent oligomerization of EspG chaperones

We studied solution structures of EspG proteins from ESX-1 ($EspG_{1mma}$), ESX-3 ($EspG_{3mma}$, $EspG_{3mtu}$, $EspG_{3msm}$) and ESX-5 ($EspG_{5mtu}$) secretion systems using SAXS (Table 3). The EspG proteins from different secretion systems have diverged significantly although the $EspG_3$ homologs from different species have a high degree of sequence identity. The Guinier analysis of the obtained SAXS profiles confirmed that the proteins were not

aggregated allowing further analysis of their structures and oligomeric states (Table 3). The dependencies of the molecular weight estimates and the excluded volume of the hydrated particles on concentration were studied for all proteins. Prior structural information of the monomeric form existed for all of the studied proteins, but experimental models of the dimeric state were only available for $EspG_{3msm}$.

SAXS measurements of $EspG_{1mma}$ at four different protein concentrations resulted in distinct scattering profiles. The molecular weight (based on the Porod volume) increased with increasing concentration from 43 to 72 kDa at 1.0 mg/mL and 6.0 mg/mL, respectively (Table 3). A similar trend was observed for the R_g and D_{max} values. The oligomer analysis of the concentration-dependent SAXS data was carried out using theoretical scattering profiles based on the monomeric $EspG_{1mka}$ (PDB ID 5VBA) structure and two different dimeric structural models. The β8-mediated dimer observed in the $EspG_{3msm}$ (PDB ID 4RCL) structure and the wing-shaped dimer structure $EspG_{3msm}$ (PDB ID 4L4W) were used as templates to generate $EspG_{1mma}$ dimer models and the corresponding theoretical scattering profiles to decompose the experimental data. (Table 4a and b). The *OLIGOMER* analysis showed that $EspG_{1mma}$ is predominantly a monomer at low protein concentrations, while the fraction of dimeric protein increases up to 50% at the highest concentration measured. However, the goodness-of-fit (χ^2) of the theoretical scattering based on linear combinations of theoretical monomer/dimer scattering profiles to the experimental SAXS data varied significantly between the two dimer models (Tables 4a and 4b). The SAXS data could not be interpreted successfully using the β8-mediated dimeric arrangement (Table 4a). Additional evidence that the β8-mediated dimer is a non-physiological crystallographic dimer is the substantial structural clashes observed when the β8-mediated $EspG_1$ dimer is superimposed onto the $EspG_{5mtu}$ structure derived from the heterotrimeric PE25–PPE41–$EspG_{5mtu}$ crystal structure (Fig. 3). The wing-shaped dimer conformation based on the $EspG_{3msm}$ (PDB ID 4L4W) crystal structure yields much better fits (Table 4b) to the measured scattering data, which strongly indicates that $EspG_1$ dimers adopt the wing-shaped conformation in solution.

The program *OLIGOMER* was also used to fit a set of theoretical scattering profiles of monomeric and dimeric $EspG_3$ models to the experimental $EspG_{3mtu}$ SAXS data. A dimer model was constructed based on the wing-shaped dimer structure of $EspG_{3msm}$ (PDB ID 4L4W). All fits at different concentrations provided good χ^2 values indicating that our wing-shaped dimer $EspG_{3mtu}$ model based on the $EspG_{3msm}$ structure is appropriate. Analysis of the volume distributions of the oligomeric states showed that even at the lowest concentration (1.1 mg/mL), 46% of the protein was in dimeric form. The dimeric protein fraction increased to 100% at the highest measured concentration (6.1 mg/mL) (Table 4c). Likewise, the volume fractions of the oligomeric states were calculated for $EspG_{3mma}$. Again the dimeric experimental structure of $EspG_{3msm}$ (PDB ID 4L4W) was used as the template to model the dimeric form of $EspG_{3mma}$. $EspG_{3mma}$ showed a similar oligomerization pattern as $EspG_{3mtu.}$ The volume fraction of the dimeric form of the protein is above 46% even at the lowest protein concentration (Table 4d).

We measured the SAXS profiles of two different $EspG_{3msm}$ protein preparations, native and selenomethionine (SeMet) incorporated forms. Interestingly, the two proteins showed distinct oligomerization behaviors. The native $EspG_{3msm}$ sample had a significant fraction of the dimeric form present already at the lowest measured concentration and the fraction stayed stable as the protein concentration increased. On the contrary, the SeMet-labeled form remained monomeric over the whole concentration range. The *CRYSOL* fit of the monomeric structure (PDB ID 4L4W) to the scattering data from the SeMet-labeled construct provided a χ^2 value of 0.93. This enabled us to use the SAXS data from the SeMet-labeled protein for *ab initio* modeling, which requires a monodisperse sample (Fig. 5). The SAXS-based *ab initio* model calculated with *DAMMIF* and the monomeric structure of SeMet-labeled $EspG_{3msm}$ (PDB ID 4L4W) are in a good agreement (normalized spatial discrepancy (NSD) = 1.1).

The SAXS profiles of the native form of $EspG_{5mtu}$, the only member of the $EspG_5$ family that was analyzed, do not show any concentration dependence over the measured range (0.9 to 6.7 mg/mL) (Supplementary Fig. S9 & Table 3). The constant molecular mass estimates suggest that $EspG_{5mtu}$ is monomeric in solution. We used the program *CRYSOL* to fit the theoretical scattering profile based on the crystal structure of the $EspG_{5mtu}$ monomer from the PE25–PPE41–$EspG_{5mtu}$ structure (PDB ID 4KXR) to the experimental SAXS data. The fit of the crystallographic structure yielded a χ^2 value of 1.2 showing a severe misfit in the range of momentum transfer of about 2.0 nm^{-1} (Fig. 7a). In order to evaluate whether flexibility of the $EspG_{5mtu}$ β2–β3 loop (Gly^{92}-Asn^{114}) might cause this discrepancy, we employed molecular dynamics (MD) simulations to assign flexible amino acid residues and ensemble optimization method (EOM) to fit the measured SAXS data (Fig. 7a). The amino acid residue Root-Mean-Square-Fluctuations (RMSF) monitored during a 2 ns production indicated high flexibility of the β2–β3 loop region (Fig. 7a). Thus, we introduced flexibility in the all the identified loop regions of $EspG_5$ with the program *EOM* and also modeled the 24 amino acid residues that were missing from the crystallographic structure. The resulting model with a flexible β2–β3 loop provides an excellent fit with the experimental SAXS data (Fig. 7a) (χ^2 = 0.99). In contrast to the original crystallographic structure in which the β2–β3 loop interacts with the PE–PPE heterodimer in an extended conformation, the EOM structures of $EspG_{5mtu}$ in solution have more compact forms. More specifically, the β2–β3 loop of monomeric $EspG_{5mtu}$ folds closely onto the protein core in the SAXS-refined solution structures (Fig. 7b). In addition, the monodisperse $EspG_{5mtu}$ SAXS data were employed for *ab initio* modeling using *DAMMIF* (Supplementary Fig. S8). The structural alignment yielded a NSD value of 0.93 indicating excellent agreement.

Taken together, these data show clear differences in the oligomerization trends of each EspG ortholog from different ESX systems, indicating that this could be another level of system specificity involved in the secretion of PE–PPE proteins via ESX systems.

PE5–PPE4–EspG$_3$ trimer structure in an extended conformation

To further analyze substrate recognition by different EspG proteins, we measured solution scattering of PE5–PPE4–EspG$_3$ and PE25–PPE41–EspG$_5$ complexes from *M. tuberculosis*. Model-free parameters derived from the SAXS data indicate that PE5–PPE4–EspG$_{3mtu}$ has a more extended open overall conformation (D_{max} =14.5 nm / R_g = 4.25 nm) than the crystallographic structure of the PE25–PPE41–EspG$_{5mtu}$ complex (D_{max} = 13.0 nm / R_g = 3.93 nm) (Fig. 8). *Ab initio* modeling in *P*1 symmetry using SAXS data provided independent information about the overall shapes. The EspG$_{3mtu}$ complex reveals a more open structure than EspG$_{5mtu}$ complex, which is consistent with the model-free parameters. In addition, the overall shape of the EspG$_{5mtu}$ complex *ab initio* structure is in agreement with the crystallographic structure showing a compact structure (PDB ID 4KXR; NSD = 1.7). Also, the theoretical scattering of the crystallographic structure of the PE25–PPE41–EspG$_{5mtu}$ complex fits the measured SAXS data very well (χ^2 = 0.95) (Fig. 9). This indicates that, in solution, the EspG$_{5mtu}$ β2–β3 loop is in the extended conformation seen in the crystal structure of the PE25–PPE41–EspG$_{5mtu}$ heterotrimer. Thus, the SAXS data for EspG$_{5mtu}$ alone and in complex with PE25–PPE41 indicates that the β2–β3 loop undergoes a significant conformational change upon binding.

In order to produce an atomic rigid body model of the PE5–PPE4–EspG$_{3mtu}$ complex, 300 decoy structures were generated using a molecular docking approach [35] and the crystallographic EspG$_{3mtu}$ (PDB ID 4W4I, [27]) structure together with homology models of a complex of full length PE5 and the N-terminal domain of PPE4 (residues 1-178) from *M. tuberculosis* generated with *SWISS-MODEL* [36]. The decoy structures were then ranked by the goodness-of-the-fit values of their theoretical scattering compared to the experimental scattering data. Fourteen complex structures were selected for further analysis on the basis of their chi^2–values (χ^2 < 1.7). In addition, all structures had acceptable fits according to *p*-values provided by the correlation map approach [37]. A representative model with the

lowest χ^2–value was selected for the comparison with the PE25–PPE41–$EspG_{5mtu}$ complex (Figs. 8 and 10).

Comparison of the crystallographic structure of PE25–PPE41–$EspG_{5mtu}$ (PDB ID 4KXR, [26]) and the SAXS-based rigid-body model of PE5–PPE4–$EspG_{3mtu}$ shows similarities in the binding interfaces of the two complexes, but also significant differences related to the overall binding orientation (Fig. 8). The interface between $EspG_{3mtu}$ and the PE5–PPE4 heterodimer was found to be mostly hydrophobic comprised of 28 amino acid residues from $EspG_3$ and 19 from PE4. Analogous to the PE25–PPE41–$EspG_{5mtu}$ complex, the loop between helices α4 and α5 of PPE4 (Ala^{125}-Ile^{134}) interacts with the central β-sheet of $EspG_3$. The structure suggests a hydrogen bonding network between $EspG_3$ and PPE4 formed by several hydrophobic, polar and charged amino acid residues (residues Trp^{27}, Glu^{196}, Glu^{211}, Ser^{215} of $EspG_{3mtu}$ and residues Thr^{126}, Phe^{128}, Gly^{130}, Asn^{132}, Thr^{133}, Ile^{134} of PE4 from *M. tuberculosis*). Based on the SAXS data and models, we suggest that the more open and flexible structure of PE5–PPE4–$EspG_3$ is due to differences in the EspG β2–β3 loop region. The $EspG_{5mtu}$ β2–β3 loop is comprised of 25 amino acid residues (Gly^{92}-Asn^{114}) and its interaction with PE25–PPE41 forms an extended interface extending from the central β-sheet of $EspG_{5mtu}$. However, the homologous loop region in $EspG_{3mtu}$ structure is significantly shorter (12 amino acid residues; Val^{87} to Leu^{98}) thus an analogous interaction is missing in the PE5–PPE4–$EspG_{3mtu}$ rigid-body model. Given that ESX-5 is the major secretion system for export of PE/PPE proteins, the length and flexibility of the $EspG_{5mtu}$ β2–β3 loop could be an important structural feature allowing $EspG_{5mtu}$ to interact specifically with many different PE–PPE heterodimers.

Conclusions

Transport of multiple proteins across the mycobacterial cell envelope is facilitated by the ESX system and cytoplasmic EspG chaperones. However, the precise recognition mechanism of the cognate substrates by ESX system-specific chaperones is not yet fully understood. In this work we present structural analyses of $EspG_1$, $EspG_3$ and $EspG_5$ and

their complexes with PE–PPE secretion substrates using a combination of experimental and *in silico* methods. The solution scattering data together with novel X-ray crystallographic structures allows us to hypothesize about the substrate specificity of EspG chaperones and provides insight into chaperone-substrate binding mechanisms. This study demonstrates that the β2–β3 loop of EspG plays an important role in PE–PPE binding and is a major differentiation factor between the EspG chaperones of orthologous ESX secretion systems. Our results also suggest that EspG dimerization may play a role in substrate recognition.

Materials and methods

Cloning, expression and purification of *M. kansasii* EspG$_1$

The DNA sequence corresponding to the full-length EspG$_{1mka}$ was PCR amplified using primers G1mka_F1Nde, 5'-GATACATATGACCGGTCCGCTCGCTAC and G1mka_R283Hind, 5'-CTCAAGCTTAGCCTCGGGCGGAGGCTTG, and genomic DNA of *M. kansasii* ATCC 12478. The PCR product was digested with NdeI/HindIII and ligated into the corresponding sites of a modified pET-28b vector to create an N-terminal His$_6$-tag with a tobacco etch virus (TEV) cleavage site. In efforts to optimize initial crystals, the Cys114Ala and Cys170Ala mutations were introduced using the QuikChange protocol (Stratagene). A truncated DNA fragment corresponding to residues 17-271 was PCR amplified using primers G1mka_F17Nco, 5'-GATTCCATGGTCGGCGTCGAGGTCACC and G1mka_R271Hind, 5'-CTCAAGCTTCAATCTAACCAGGAGCCCGC and cloned into a pET-based vector containing an N-terminal His$_6$-tag followed by a TEV cleavage site and T4L sequence (residues 2-162). The T4L sequence corresponds to a cysteine-less variant with Cys54Thr and Cys97Ala mutations [38, 39]. T4L-EspG$_{1mka}$ was expressed in *E. coli* Rosetta2(DE3) cells in LB supplemented with 50 μg mL^{-1} kanamycin and 34 μg mL^{-1} chloramphenicol. Cells were grown at 37ºC and expression was induced with 0.5 mM IPTG at A_{600} of 0.6. Cells were harvested by centrifugation after 3 h, resuspended in lysis buffer (20 mM Tris-HCl pH 8.5, 300 mM NaCl, 10 mM imidazole) and lysed using an EmulsiFlex C5 homogenizer

(Avestin). $EspG_{3msm}$ was purified via Ni-NTA metal affinity chromatography. The His_6-tag was cleaved using TEV protease followed by a second Ni-NTA purification step to remove uncleaved T4L-$EspG_{1mka}$ and His_6-tagged TEV protease. Size-exclusion chromatography was performed using a Superdex 200 column (GE Biosciences) equilibrated in buffer containing 20 mM HEPES pH 7.5, 300 mM NaCl.

Crystallization and structure solution of T4L-$EspG_{1mka}$

Crystals of T4L-$EspG_{1mka}$ were obtained by the hanging drop vapor diffusion method using crystallization solution containing 0.1 M Bicine pH 9.0, 1.0 M LiCl, 10% PEG6000. The crystals were cryoprotected in crystallization solution supplemented with 20% glycerol and flash cooled in liquid nitrogen before data collection. Data were collected at the SER-CAT beamline 22-ID at the Advanced Photon Source, Argonne National Laboratory. Data were processed and scaled using *XDS* and *XSCALE* [40]. The T4L-$EspG_{1mka}$ structure was solved by molecular replacement using *Phaser* [41], with the T4L structure (PDB 4GBR) [42] and poly-Ala $EspG_{3msm}$ (PDB ID 4L4W) structure as search models. Two copies of T4L-$EspG_{1mka}$ were located in the asymmetric unit. Density modification was performed using *Parrot* [43], and the molecular replacement model was re-built using *Buccaneer* [44, 45], *ARP/wARP* [46] and manual building in *Coot* [47]. The iterative rounds of refinement and re-building were performed using *phenix.refine* [48] and *Coot*. Non-crystallographic symmetry (NCS) restraints were applied throughout the refinement. Statistics for data collection, refinement, and model quality are listed in Table 1.

Cloning, expression, and purification of *M. marinum* $EspG_3$

The gene (MMAR_0548) encoding $EspG_{3mma}$ was PCR-amplified from *M. marinum* M genomic DNA with Phusion DNA polymerase (New England Biolabs) using gene specific primers (MMAR_0548.For, 5'-AACCTGTATTTCCAGAGTATGGAGTCAATGCCCAACG and MMAR_0548.Rev, 5'-ttcgggctttgttagcagttaGGAGGGTTGACTCGAGAAATCT) and was cloned into a modified pET28 vector, pMAPLe4 [49], using the Gibson ISO assembly

procedure [50]. The DNA sequence of the construct was verified by DNA sequencing (Genewiz). $EspG_{3mma}$ was expressed from pMAPLe4 as a maltose binding protein (MBP) fusion which was cleaved *in vivo* from MBP via a tobacco vein mottling virus (TVMV) protease cleavage site situated between the two moieties; a His_6 affinity tag and a tobacco etch virus (TEV) protease cleavage site is encoded in the linker between the TVMV protease cleavage site and the N-terminus of the target protein. $EspG_{3mma}$ was expressed in *E. coli* BL21-Gold (DE3) (Agilent Technologies) using Terrific broth media and protein expression was induced with 1 mM IPTG at 18°C overnight. Harvested cells were resuspended in lysis buffer (20 mM Tris, pH 8.0, 300 mM NaCl, 10% glycerol, 10 mM imidazole) supplemented with β-mercaptoethanol (2 mM), DNase I, lysozyme, and Complete protease inhibitor cocktail (Roche) and lysed by sonication. The lysate was centrifuged (39,000 *g*, 30 minutes, 4°C) and $EspG_{3mma}$ was purified from the clarified supernatant using Ni-NTA resin (Thermo Fisher Scientific) equilibrated in lysis buffer. The bound protein was eluted with lysis buffer containing 300 mM imidazole and further purified by size exclusion chromatography (SEC) using a HiLoad 16/60 Superdex 75 column (GE Healthcare) equilibrated with 20 mM Tris, pH 8.0, 300 mM NaCl, 10% glycerol. $EspG_{3mma}$ eluted from the column in a single symmetrical peak which was concentrated to 21.5 mg mL^{-1} for crystallization screening.

Crystallization and structure determination of $EspG_{3mma}$

Small crystals of $EspG_{3mma}$ were grown using the hanging drop vapor-diffusion method by mixing 1 µL of protein with 0.5 µL of reservoir solution (1.4 M ammonium sulfate, 200 mM lithium sulfate, 60 mM CAPS, pH 10.5). These small crystals were used to streak seed other drops that had been equilibrated for a week but showed no signs of crystal growth. Large crystals were found in seeded drops with a reservoir solution containing 1.45 M ammonium sulfate, 200 mM lithium sulfate, 70 mM CAPS, pH 10.5 after 5 weeks. For phase determination and cryoprotection crystals were soaked for 30 minutes at room temperature in a solution containing approximately 4 mM platinum potassium thiocyanate, 1.17 M ammonium sulfate, 160 mM lithium sulfate, 56 mM CAPS pH 10.5, and 15.5% glycerol.

Diffraction data were collected at the Advanced Photon Source at Argonne National Laboratory on beamline 24-ID-C. The data were processed with *XDS* [40], and the structure was solved by single wavelength anomalous dispersion using *HKL2MAP* [51], in the *SHELX* suite of programs [52], which determined the position of seven platinum atoms in the $K_2Pt(SCN)_6$–soaked crystal. An initial model was built using *SHELXE* [53] which was improved through iterative rounds of manual model building using *Coot* [47] interspersed with refinement using *REFMAC*5 [54].

Cloning, expression and purification of *M. smegmatis* $EspG_3$

The gene *msmeg_0622* encoding $EspG_{3msm}$ was PCR amplified from genomic DNA of *M. smegmatis* mc^2155 using primers MsmG3_F1Nde, 5'-GAGACATATGGGGCCTAACGCTGTTG, and MsmG3_R293Hind, 5'-CTCAAGCTTACTAGTCATGCTTTCTGGGTTCTTCTCTG. The PCR product was digested with NdeI/HindIII and ligated into the corresponding sites of a modified pET-28b vector to create TEV protease-cleavable N-terminal His_6-tag fusion. The construct was verified by DNA sequencing (Eurofins Genomics). $EspG_{3msm}$ was expressed and purified using procedures similar to the T4L-$EspG_{1mka}$ fusion, except the final SEC step was performed in buffer containing 20 mM HEPES pH 7.5, 100 mM NaCl.

Crystallization and structure solution of $EspG_{3msm}$

Crystals of $EspG_{3msm}$ in space group $P3_221$ were obtained by hanging drop vapor diffusion method with crystallization solutions containing 0.1 M Tris-HCl pH 7.0, 0.2 M Mg acetate, 1.8 M NaCl (SeMet substituted $EspG_{3msm}$) and 0.1 M HEPES pH 7.4, 1.0 M LiCl, 10% PEG6000 (native $EspG_{3msm}$). Crystals were transferred to crystallization solutions supplemented with 20-25% glycerol and flash-cooled in liquid nitrogen prior to data collection. Data for native and SeMet substituted $EspG_{3msm}$ crystals were collected at the SER-CAT beamline 22-ID at the Advanced Photon Source, Argonne National Laboratory. Data were processed and scaled using *XDS* and *XSCALE* [40]. The $EspG_{3msm}$ structure was solved by SeMet-SAD.

The initial selenium positions were found with *SHELXD* [52] using *HKL2MAP* interface [51]. Phasing, density modification and initial model building was performed using autoSHARP [55]. A partial model was refined against a native dataset and rebuilt using *REFMAC*5 [54], *ARP/wARP* [46] and AutoBuild within *PHENIX* [56]. The model was completed by iterative rounds of refinement and rebuilding using *phenix.refine* [48] and *Coot* [47].

Crystals of SeMet substituted $EspG_{3msm}$ in space group $C222_1$ were grown using crystallization solution containing 0.1 M Tris-HCl pH 8.5, 1.0 M LiCl, 20% PEG6000. Crystals were transferred into crystallization solution supplemented with 20% glycerol and flash cooled in liquid nitrogen. The structure was solved by molecular replacement using *Phaser* [41] with $EspG_{3msm}$ (PDB ID 5SXL) structure as a search model. Two $EspG_{3msm}$ molecules were located in the asymmetric unit. Following density modification using *Parrot* [43], the molecular replacement model was rebuilt using *Buccaneer* [44, 45]. The model was further improved using *Coot*, *ARP/wARP* and AutoBuild within *PHENIX*. The final model was refined using *phenix.refine*.

Crystals of $EspG_{3msm}$ in space group $P4_32_12$ were grown using crystallization solution containing 0.1 M Na cacodylate pH 6.0, 15% PEG200, 5% PEG3350. The crystals were cryoprotected in solution containing 0.1 M Na cacodylate pH 6.0, 35% PEG200, 5% PEG3350 and flash cooled in liquid nitrogen. Molecular replacement using *Phaser* and $EspG_{3msm}$ (PDB ID 4L4W) structure as a search model located 2 molecules in the asymmetric unit. The model was refined using *REFMAC*5 and rebuilt using AutoBuild within *PHENIX*. The iterative rounds of refinement and rebuilding were performed using *phenix.refine* and *Coot*. NCS restraints were applied in early rounds of refinement and were later omitted as the model quality improved. The last several rounds of refinement were performed using 4 translation/libration/screw (TLS) groups, identified by the TLSMD server [57, 58], per protein chain.

Sample preparation for SAXS measurements

The gene MMAR_5441 encoding $EspG_{1mma}$ was PCR amplified from genomic DNA of *M. marinum E11* using primers DF018, 5'ATATATAGATCTACCGGTCCGCTCGCTACCGG', and DF019, 5'-ATATATATGCGGCCGCTTAACCTCGGGCGGTGGCGTCG'. The PCR product was digested with BglII/NotI. The gene MMAR_0548 encoding $EspG_{3mma}$ was PCR amplified from genomic DNA of *M. marinum E11* using primers DF020, 5' ATATATACCGGTGGAATGGAGTCAATGCCCAACGC', and DF021, 5'-ATATATATGCGGCCGCTTAGGAGGGTTGACTCGAGAA'. The PCR product was digested with AgeI/NotI. Clones containing genes Rv0289 and Rv1794 encoding $EspG_{3mtu}$ and $EspG_{5mtu}$ were further digested with BglII/NotI and AgeI/NotI. Digested fragments were ligated into the corresponding sites of pETM11-SUMO3 to create SENP-2 protease-cleavable N-terminal His_6-$SUMO_3$-tag fusions.

His_6-$SUMO_3$-$EspG_{1mma}$, His_6-$SUMO_3$-$EspG_{3mma}$, His_6-$SUMO_3$-$EspG_{3mtu}$ and His_6-$SUMO_3$-$EspG_{5mtu}$ proteins for SAXS measurements were purified as follows: cells were resuspended in lysis buffer 20 mM HEPES pH 7.5, 150 mM NaCl, 10 mM imidazole, 0.25 mM tris(2-carboxyethyl)phosphine (TCEP), 10% (w/v) glycerol (pH 7.5) containing 1/100 protease inhibitor mix HP (Serva), DNAse I (10 µg/ml) and disrupted by lysozyme treatment followed by sonication. The protein was purified via Ni-NTA (Qiagen) affinity chromatography. His6-$SUMO_3$-tag was cleaved by $SenP_2$ protease and further purified using a Phenyl Sepharose HP column (GE Biosciences), followed by SEC using a Superdex 200 16/60 column (GE Biosciences) pre-equilibrated with 20 mM HEPES pH 7.5, 150 mM NaCl, 0.25 mM TCEP, 10% (w/v) glycerol.

The purification procedure for the PE25-PPE41-His_6-$EspG_{5mtu}$ complex was the same as for the His_6-$SUMO_3$-EspG proteins described above with the exception that the cleavage of the His6 tag was performed by addition of TEV protease. For final aggregated protein removal, the complex was concentrated and injected into a Superdex 200 16/60 size-exclusion chromatography column (GE Biosciences) pre-equilibrated with 20 mM HEPES pH 7.5, 150 mM NaCl, 0.25 mM TCEP, 10% (w/v) glycerol. All samples used for SAXS experiments were concentrated to the appropriate protein concentrations ranging from ~1–7 mg ml^{-1}.

SAXS measurements

SAXS measurements were carried out at beamline P12 (EMBL/DESY, Hamburg) [59] at the PETRA-III storage ring using a Pilatus 2M detector (Dectris). Measurements for the purified proteins were made at several concentrations (Table 4). For each measurement twenty 50 ms exposure frames were collected and averaged using a sample volume of 30 µl at a temperature of 10°C. The SAXS camera was set to a sample-detector distance of 3.1 m, covering the momentum transfer range 0.008 Å-1 < s < 0.47 $Å^{-1}$ ($s = 4\pi \sin(\theta)/\lambda$ where 2θ is the scattering angle and λ=1.24 Å is the X-ray wavelength). Prior to and following each sample exposure, a buffer control was measured to allow for background subtraction.

SAXS data analysis using model-free parameters

Radius of gyration R_g and forward scattering intensity $I(0)$, were independently determined using Guinier analysis [60] and the indirect Fourier transformation approach of the program GNOM [61]. Additionally, the maximum particle dimension D_{max} was obtained from the latter approach. Molecular masses of protein constructs (MM_{SAXS}) were calculated by comparing the extrapolated forward scattering intensities with that of a reference BSA sample (MM_{ref} = 66 kDa) together with concentration information. The excluded volume of the hydrated protein Vp was obtained with DATPOROD [62] and used to extract an independent estimate of molecular mass (MM_{POROD}). For globular proteins, hydrated protein volumes in $Å^3$ are approximately 1.7 times the molecular masses in Dalton.

SAXS-based structural modeling

Ab initio models were reconstructed from the scattering data using the simulated annealing based bead-modeling program *DAMMIF* [63]. Ten independent reconstructions were averaged to generate a representative model with the program *DAMAVER* [64]. In addition, the average *DAMMIF ab initio* model was used to calculate an excluded volume of the particle, V_{DAM}, from which an additional independent MM estimate can be derived

(empirically, $MM_{DAM} \sim V_{DAM}/2$). The resolutions of the model ensembles were estimated by a Fourier Shell correlation approach [65].

Theoretical scattering profiles from available high-resolution crystallographic structural models were calculated using the program *CRYSOL* [66] and used to determine the fit of these models to the experimental scattering data. Given the atomic coordinates of a structural model, *CRYSOL* minimizes the discrepancy between the experimental and theoretical scattering intensities by adjusting the excluded volume of the particle and the contrast of the hydration layer. Rigid-body modeling was performed using the *ZDOCK* docking approach [35] to generate decoy structures and complexes were ranked based on their fit to the experimental scattering data.

The scattering profile from a molecular mixture can be deconvoluted into a linear combination of individual contributions $I_i(s)$ from the different species. If the structures of the components are known or their individual scattering profiles can be measured, the volume fractions of the species that fit the SAXS data can be determined by the program *OLIGOMER* utilizing nonnegative least-squares fitting [67]. Dimeric structures of $EspG_3$ from *M. tuberculosis* and *M. marinum* were generated from their monomeric crystallographic structures (PDB IDs 4W4I and 5DBL, respectively) using the *M. smegmatis* $EspG_3$ dimer structure (PDB ID 4L4W) as an interaction template. We also used the program *OLIGOMER* [67] for fitting of experimental scattering profiles of $EspG_{3mtu}$ and $EspG_{3mma}$ by weighted combinations of theoretical form factors from the monomeric crystallographic structures and dimeric models. In the case of $EspG_{3msm}$, theoretical form factors based on the dimeric and monomeric crystallographic structures (PDB ID 4L4W) were used as inputs for *OLIGOMER*. For $EspG_{1mma}$, two different dimeric structures were tested: the first dimer structure is based on the structure of the $EspG_{1mka}$ dimer (PDB ID 5VBA) while the second model for a $EspG_{1mma}$ dimer was constructed using the $EspG_{3msm}$ dimer structure (PDB ID 4L4W) as a template.

Flexibility analyses of protein structures in solution were conducted using their crystallographic structures as starting points for the ensemble optimization method (EOM).

This approach seeks to best fit the experimental scattering profile with an ensemble of conformations [68, 69]. Possible conformations of loop regions were modeled with the program *RANCH* producing 10,000 random configurations, while the rest of the protein was kept fixed. A genetic algorithm was employed to find the set of conformations best fitting the SAXS data. The structures selected from the random pool of structures were analyzed with respect to the R_g distribution.

Molecular dynamics simulations

The program NAMD was employed with CHARMM27 force field for description of the protein and the TIP3P solvent model for water. Constant particle number, constant pressure and constant temperature (*NpT*) ensembles were assumed [70-72]. *Langevin* dynamics were used to maintain constant temperature. Pressure was controlled using a hybrid *Nose-Hoover Langevin* piston method. An in-house computational pipeline for high-throughput MD simulations and the visualization program *VMD* were used to prepare input files and to analyze the simulation trajectories [73].

Accession numbers

The structure factors and atomic coordinates have been deposited in the Protein Data Bank under accession codes 5VBA (T4L-$EspG_{1mka}$), 5DLB ($EspG_{3mma}$), 4L4W, 4RCL and 5SXL ($EspG_{3msm}$).

Acknowledgements

We thank Marcel Behr for providing *M. kansasii* genomic DNA, Wilbert Bitter for providing *M. marinum* genomic DNA and Carlo Carolis for the $espG_{3mtu}$ clone. We thank the staff of the UCLA-DOE Institute Protein Expression Technology Center, supported by the U.S. Department of Energy, Office of Biological and Environmental Research (BER) program under Award Number DE-FC02-02ER63421, and the UCLA Crystallization Core for assistance in protein purification and crystallization screening. Authors thank staff members

of beamline 24-ID-C, and Southeast Regional Collaborative Access Team (SER-CAT) at the Advanced Photon Source, Argonne National Laboratory, for assistance during data collection. Use of the Advanced Photon Source was supported by the U. S. Department of Energy, Office of Science, Office of Basic Energy Sciences, under Contract No. W-31-109-Eng-38. We acknowledge the Sample Preparation and Characterization (SPC) facility of EMBL at PETRA3 (DESY, Hamburg) for technical support. Work performed in the laboratory of D.E. is supported by the Howard Hughes Medical Institute and National Institutes of Health grants 23616-002-06 F3:02, TBSGC P01 (AI068135), and TBSGC P01 (AI095208). Research reported in this publication was partially supported by an Institutional Development Award (IDeA) from the National Institute of General Medical Sciences of the National Institutes of Health under grant numbers P20GM103486 and P30GM110787, and by the National Institute of Allergy and Infectious Diseases grant number R01AI119022 to KVK. ATT was supported by the EMBL EIPOD program under Marie Curie COFUND actions and by the Bundesministerium für Bildung and Forschung (BMBF) project BIOSCAT (grant 05K12YE1).

Figures

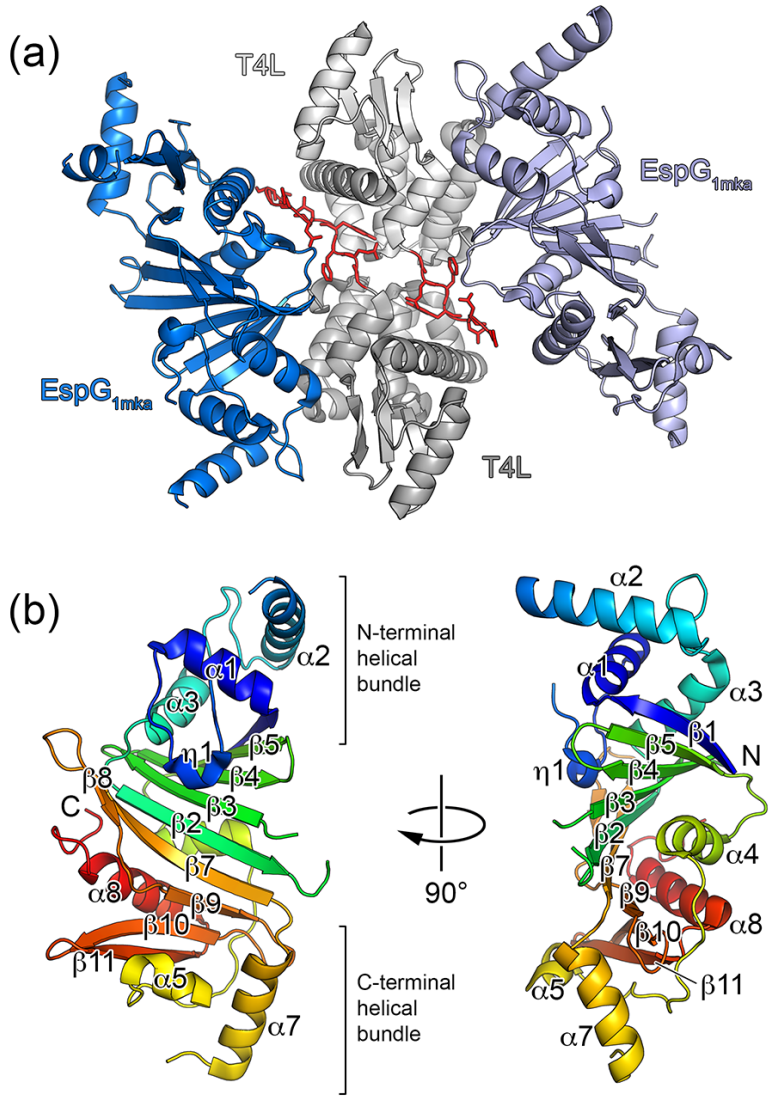

Figure 1. Structure of *M. kansasii* EspG$_1$ (EspG$_{1mka}$) (a) View of the two subunits of the T4L-EspG$_{1mka}$ fusion protein in the asymmetric unit. Chain A is shown in light grey (T4L) and light blue (EspG$_{1mka}$), and chain B is shown in dark grey (T4L) and blue (EspG$_{1mka}$). Residues corresponding to the TEV cleavage sequence are shown in red with side chains in stick representation. (b) A monomer of EspG$_{1mka}$ is shown in ribbon representation colored in rainbow colors from N-terminus (blue) to C-terminus (red). The N-terminal T4L fusion moiety is not shown for clarity.

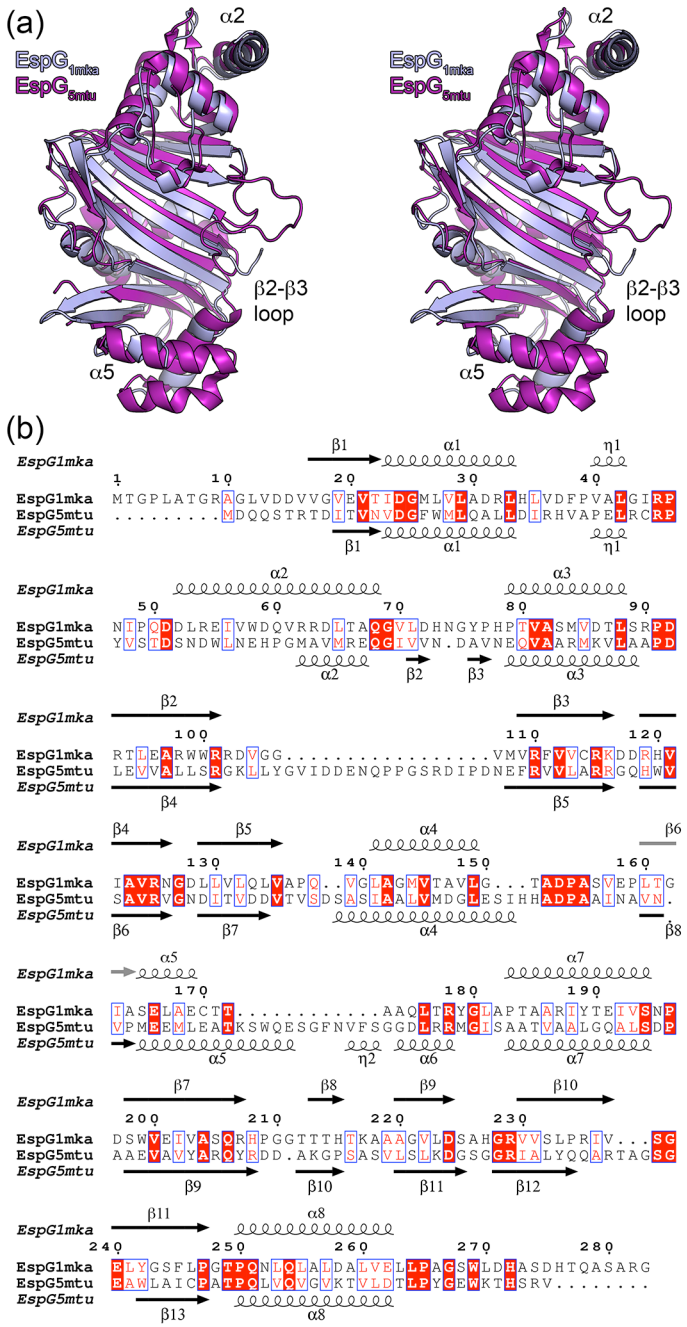

Figure 2. Structural comparison between EspG$_{1mka}$ and EspG$_{5mtu}$. (a) A stereo view of the structural superposition of the EspG$_{1mka}$ and EspG$_{5mtu}$ crystal structures. The structure of the EspG$_{5mtu}$ monomer is derived from the trimeric PE25–PPE41–EspG$_{5mtu}$ complex (PDB ID 4KXR, [26]). (b) Structure-based sequence alignment of EspG$_{1mka}$ and EspG$_{5mtu}$. Secondary structure elements corresponding to the EspG$_{1mka}$ structure (PDB ID 5VBA) and EspG$_{5mtu}$ structure (PDB ID 4KXR) are displayed above and below the alignment.

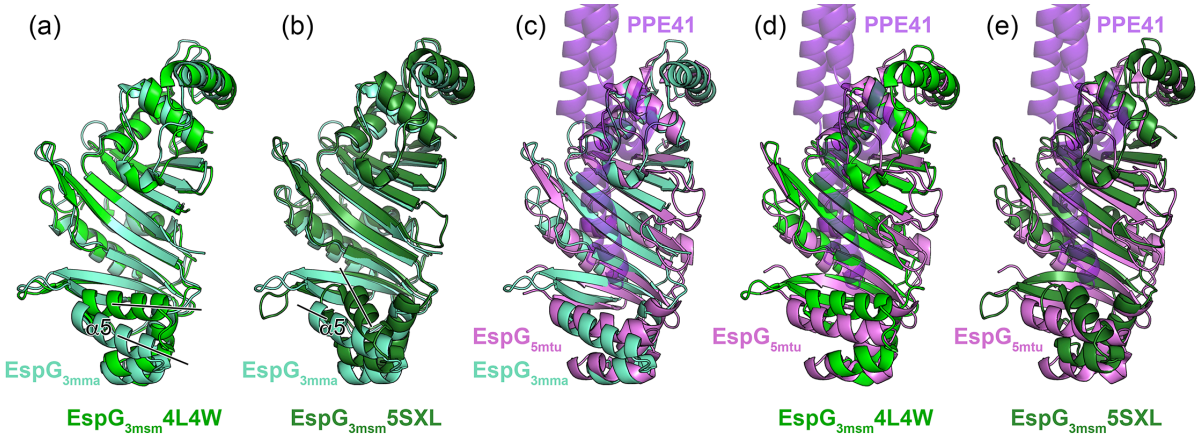

Figure 3. Structures of $EspG_3$ chaperones display variations in the putative PE-PPE binding region. (a) Structural superposition of $EspG_{3mma}$ (aquamarine) and $EspG_{3msm}$ (PDB ID 4L4W, green). Black lines indicate differences in the orientation of the α5 helix. A stereo version is available as Fig. S4a. (b) Structural superposition of $EspG_{3mma}$ and $EspG_{3msm}$ (PDB ID 5SXL, dark green). A stereo version is available as Figure S4b. (c,d,e) Structural superposition of $EspG_{3mma}$, $EspG_{3msm}$ (PDB ID 4L4W), and $EspG_{3msm}$ (PDB ID 5SXL) with $EspG_{5mtu}$ (PDB ID 4W4I [27],violet) from the PE25-PPE41-$EspG_{5mtu}$ heterotrimer crystal structure (PDB ID 4KXR [26]). PPE41 (purple) is shown in semi-transparent ribbon representation. PE25 is omitted for clarity as it is not in contact with $EspG_{5mtu}$. Stereo versions of (c,d,e) are available as Figure S5.

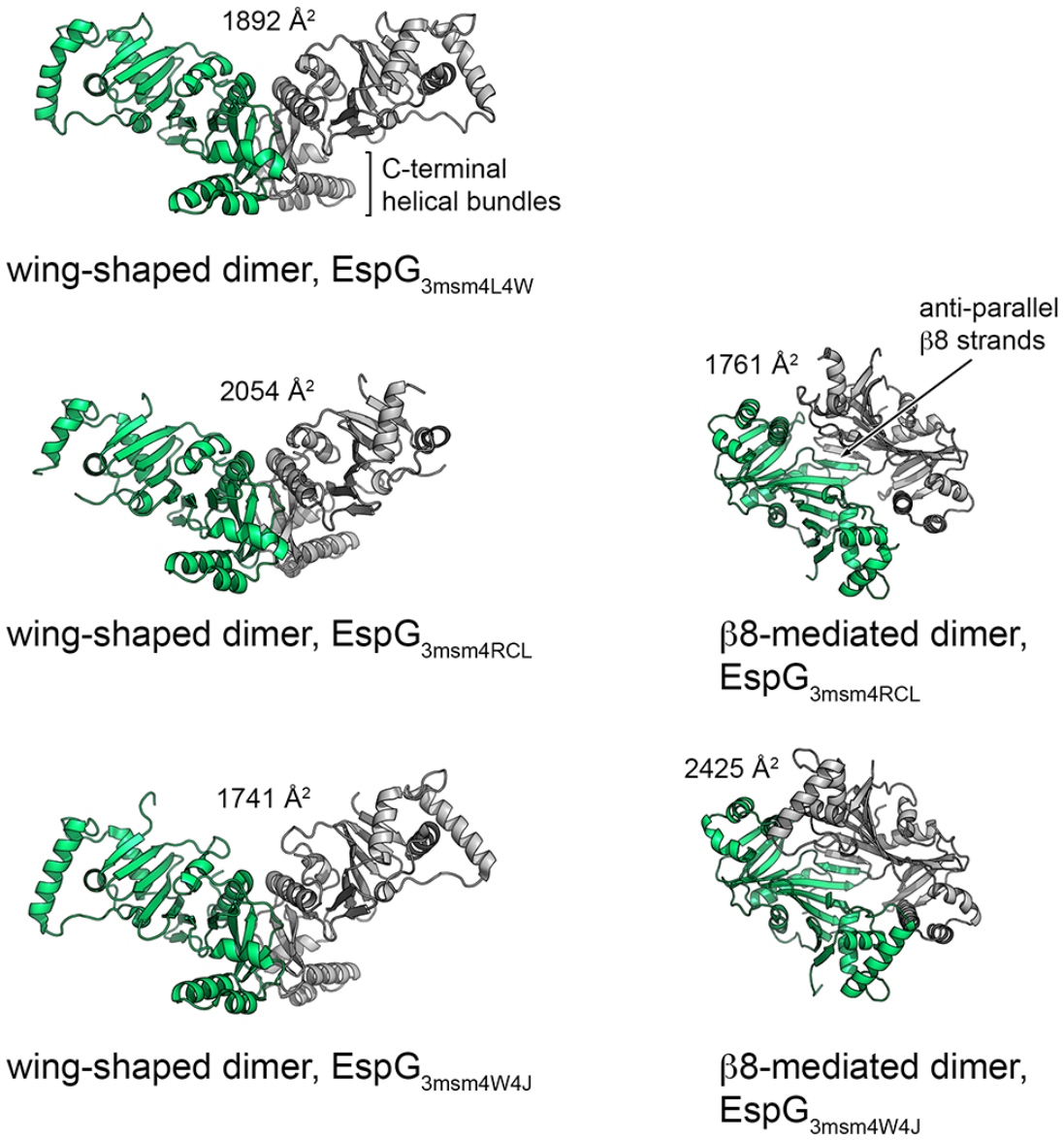

Fig. 4. Cartoon representation of the common dimer structures observed in several crystal forms of $EspG_3$. The superimposed subunits are in green. The buried surface area of the dimer interface is indicated above the structure. The wing-shaped dimers are present in the asymmetric unit in $EspG_{3msm}$ (PDB ID 4L4W) and $EspG_{3msm}$ (PDB ID 4W4J) or generated by crystallographic symmetry in $EspG_{3msm}$ (PDB ID 4RCL). The β8-mediated dimer is present in the asymmetric unit in $EspG_{3msm}$ (PDB ID 4RCL) and generated by crystallographic symmetry in $EspG_{3msm}$ (PDB ID 4W4J [27]).

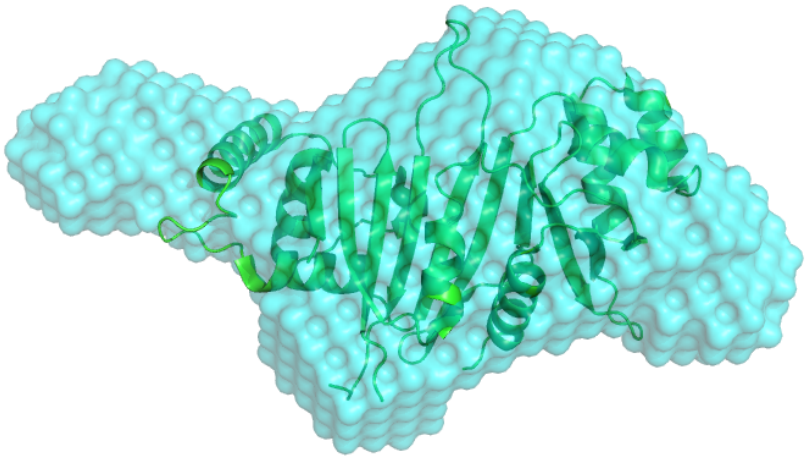

Figure 5. Structural alignment of the *DAMMIF ab initio* model (turquoise surface) and the monomeric crystallographic structure of SeMet-$EspG_{3msm}$ (PDB ID 4L4W) (green cartoon) (NSD = 1.1).

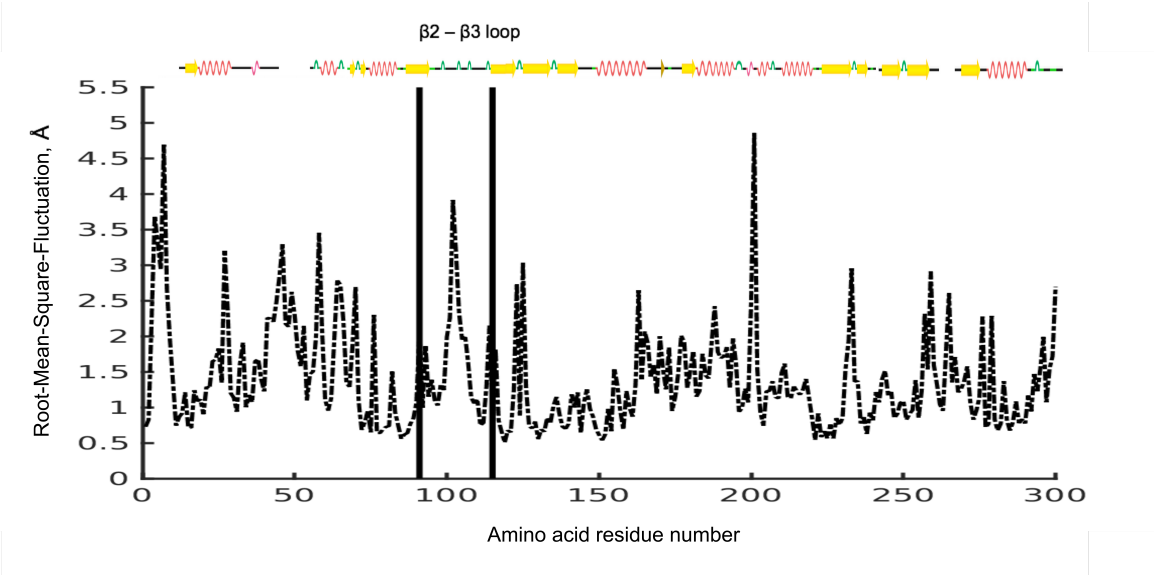

Figure 6. The amino acid residue root-mean-square-fluctuation (RMSF) of $EspG_{5mtu}$ (starting structure PDB ID 4KXR, chain C) during a MD simulation run. The secondary structure assignment of the crystallographic structure is shown above the RMSF plot for reference.

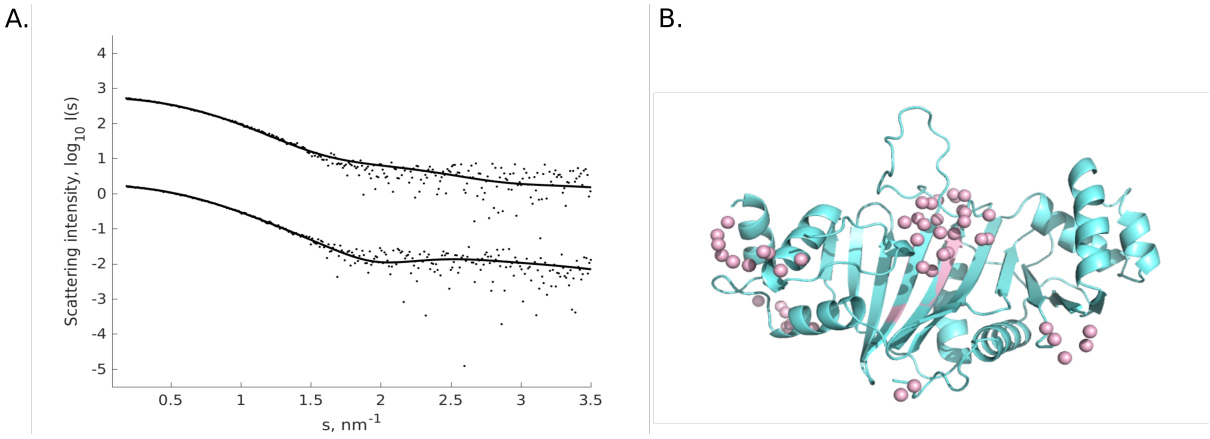

Figure 7. Solution structure of $EspG_{5mtu}$. (a) *CRYSOL* fit of the $EspG_{5mtu}$ crystal structure (PDB ID 4KXR, chain C) to the SAXS data (goodness-of-fit χ^2 = 1.2) with an apparent misfit around s = 1.8 – 2.0 nm^{-1} (above). The EOM fit with added 24 N-terminal amino acid residues that are missing from the crystallographic structure and by allowing loop flexibility shows an improved fit (χ^2 = 1.0). (b) The β2–β3 loop of $EspG_{5mtu}$ (Gly^{92}–Asn^{114}) folds closely on the protein core of $EspG_{5mtu}$ in the SAXS-refined solution structures (based on PDB ID 4KXR, chain C, cyan cartoon presentation). The flexible loop regions and the amino acid residues missing from the crystallographic structure are modeled as dummy residues (pink spheres).

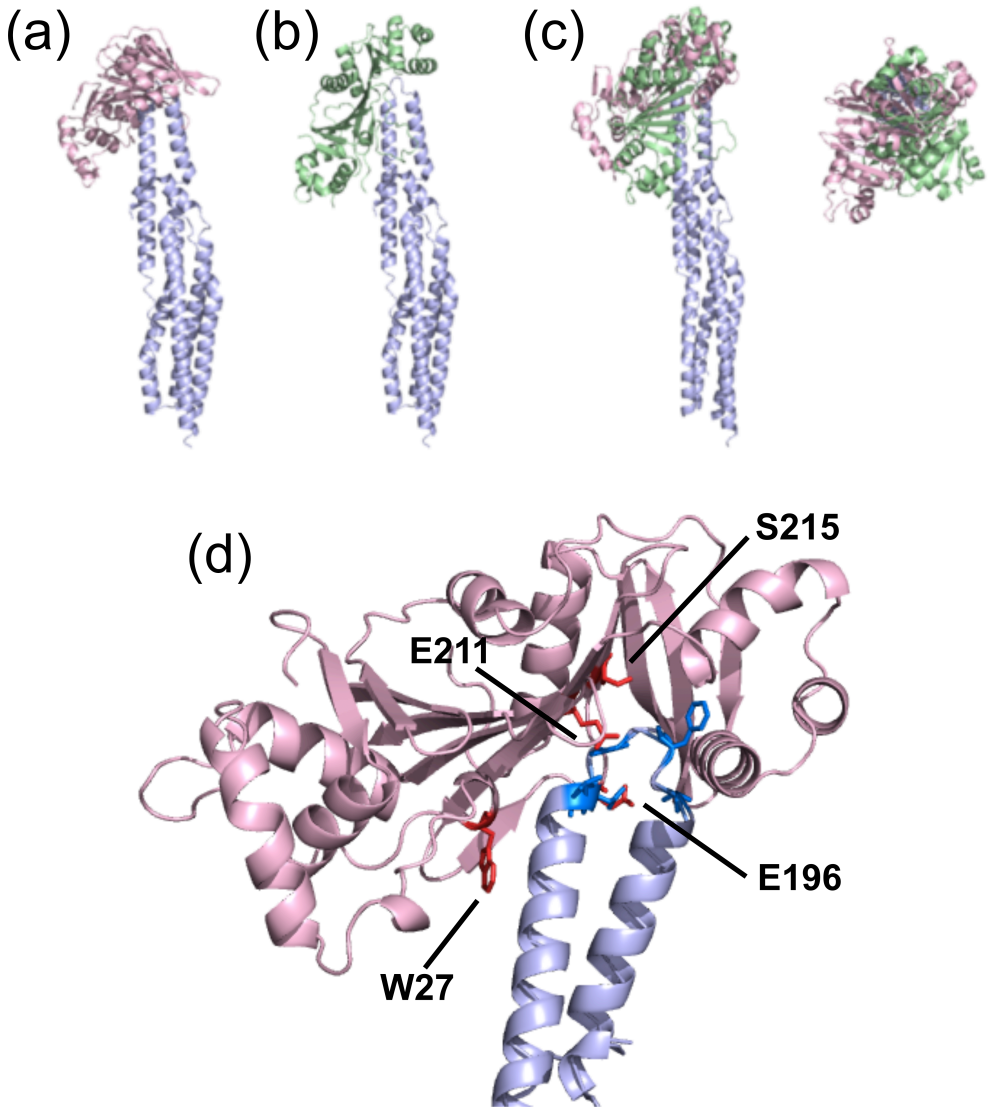

Figure 8. Comparison of PE–PPE–EspG trimer structures. (a) The crystallographic structure of $EspG_{5mtu}$ (PDB ID 4KXR, green) in complex with PE25–PPE41 (light blue) (b) The SAXS-derived rigid body model of $EspG_{3mtu}$ (pink) in complex with a homology model of PE5–PPE4 (light blue). (c) Superposition of $EspG_{5mtu}$ and $EspG_{3msm}$ in complex with a model of PE5/PPE4$^{1-178}$ (d) The interface between $EspG_{3mtu}$ and PPE4$^{1-178}$. Contact residues in the interface are colored in red ($EspG_{3mtu}$) and in blue (PPE4). The residues in PPE4 predicted to interact with the central β-sheet of $EspG_{3mtu}$ are part of the loop between helices α4 and α5 (Ala^{125}–Ile^{134}) (shown in blue).

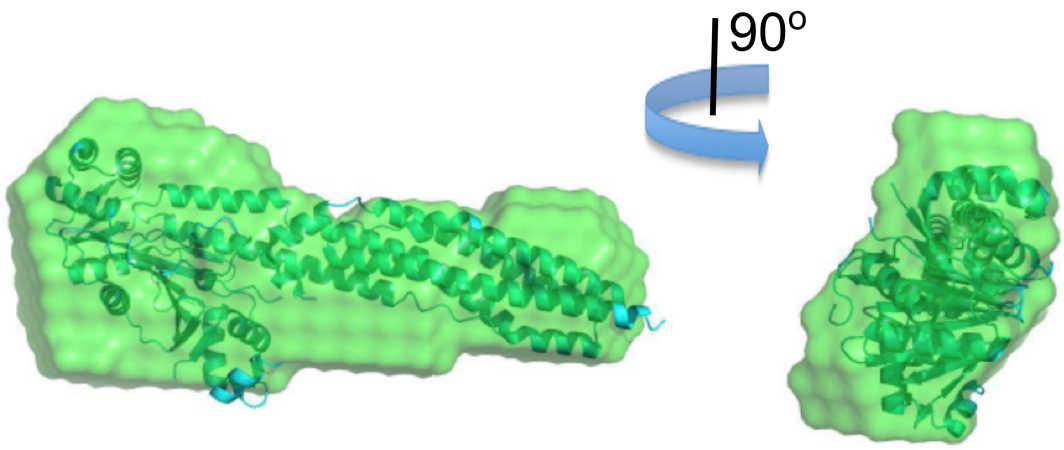

Figure 9. Fit of the SAXS *ab initio* model (green surface) and the rigid-body model of $EspG_{3mtu}$ in complex with a homology model of PE5–PPE4$^{1-178}$ (turquoise cartoon).

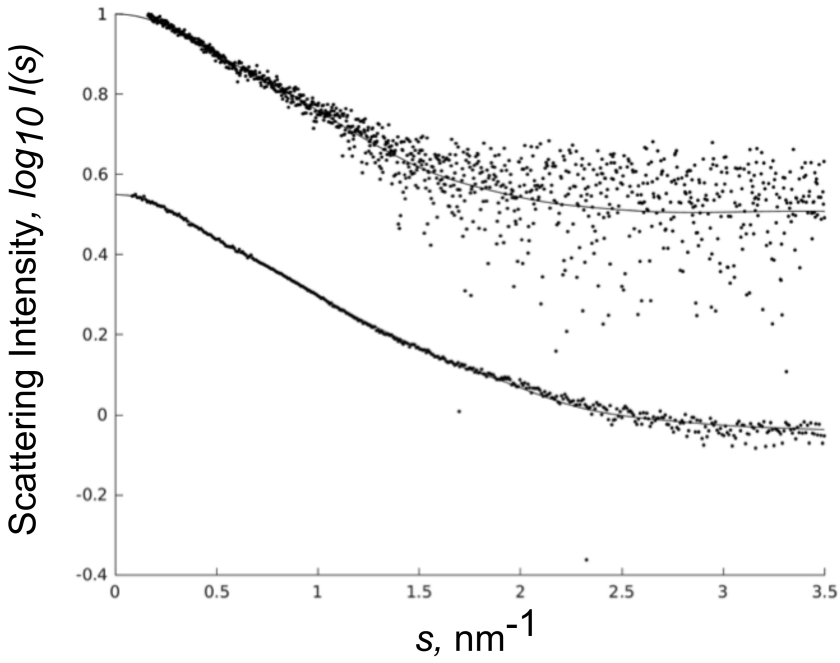

Figure 10. Fit of the PE25–PPE41–$EspG_{5mtu}$ complex structure (PDB ID 4KXR) to the experimental SAXS data (upper curve) and the fit of the $EspG_{3mtu}$ rigid-body model in complex with a homology model of PE5/$PPE4^{1-178}$ to the experimental SAXS data (lower curve). The goodness-of-fit values are X^2 = 0.939 and 1.40, respectively.

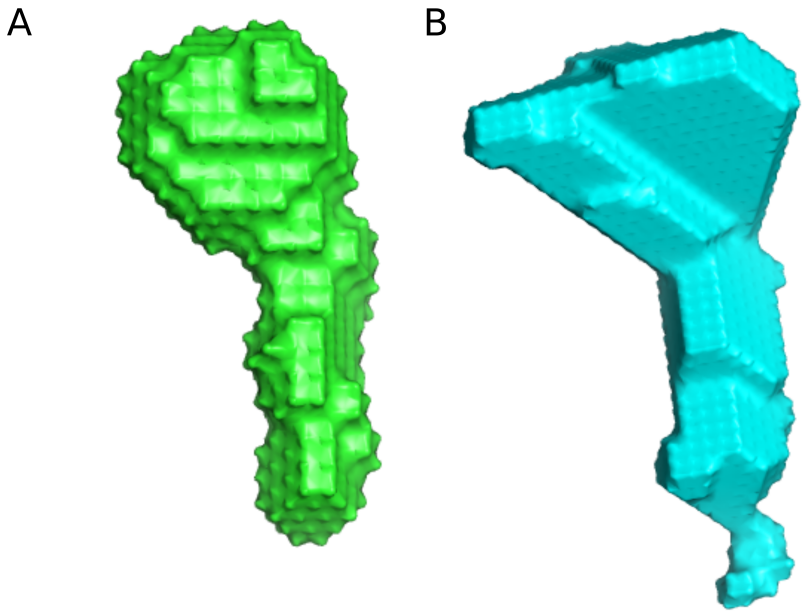

Figure 11. SAXS-based *ab initio* models of the PE25–PPE41–$EspG_{5mtu}$ complex (green) compare to the PE5–$PPE4^{1-178}$–$EspG_{3mtu}$ complex (turquoise).

Table 1. Data collection and refinement statistics.

	T4L-EspG$_1$ *M. kansasii* PDB 5VBA	EspG$_3$ *M. marinum* PDB 5DLB	EspG$_3$ *M. smegmatis* PDB 4L4W	EspG$_3$ *M. smegmatis* PDB 4RCL	EspG$_3$ *M. smegmatis* PDB 5SXL
Data collection					
Wavelength (Å)	1.0000	1.0702	0.9793	1.0000	1.0000
Space group	$P2_12_12_1$	$C2$	$C222_1$	$P4_32_12$	$P3_221$
Cell dimensions:					
a, *b*, *c* (Å)	64.14, 81.69, 160.02	112.21, 46.02, 58.01	47.08, 123.69, 180.85	92.68, 92.68, 158.85	59.15, 59.15, 183.1
α, β, γ (°)	90, 90, 90	90, 92.24, 90	90, 90, 90	90, 90, 90	90, 90, 120
Resolution (Å)	59.54–2.27 (2.33–2.27)[a]	57.96–1.77 (1.87–1.77)	45.21–2.04 (2.09–2.04)	46.34–2.70 (2.77–2.70)	39.24–2.46 (2.52–2.46)
R_{sym}	0.097 (1.110)	0.066 (0.827)	0.087 (0.809)	0.087 (1.600)	0.075 (0.882)
$CC_{1/2}$[b]	99.7 (58.3)	99.5 (65.9)	99.7 (64.6)	99.9 (76.2)	99.8 (79.3)
$I / \sigma I$	11.1 (1.74)	12.6 (1.40)	12.2 (1.55)	19.8 (1.92)	12.2 (1.62)

Completeness (%)	99.8 (100.0)	89.0 (90.0)	97.6 (79.5)	99.8 (98.5)	98.6 (99.8)
Multiplicity	6.3 (6.5)	3.2 (3.4)	5.5 (3.1)	11.1 (11.2)	5.4 (5.5)
Refinement					
Resolution (Å)	59.54–2.27	57.96–1.77	45.21–2.04	46.34–2.70	39.24–2.46
No. reflections (total / free)	39576 / 1882	24426 / 1310	33548 / 1682	19765 / 1008	13963 / 707
R_{work} / R_{free}	0.214 / 0.251	0.209 / 0.245	0.186 / 0.231	0.230 / 0.278	0.206 / 0.247
Number of atoms:					
Protein	6288	1944	4003	3709	2078
Ligand/ion	10	140			
Water	56	65	225	14	17
B-factors:					
Protein	61.6	37.8	37.9	92.1	81.7
Ligand/ion	68.1	72.7			
Water	48.5	47.1	39.3	40.6	63.4
All atoms	61.5	40.4	38.0	91.9	81.6
Wilson *B*	47.8	38.0	37.2	74.7	67.6
R.m.s. deviations:					

Bond lengths (Å)	0.004	0.019	0.008	0.003	0.002
Bond angles (°)	0.657	2.130	1.166	0.722	0.494
Ramachandran distribution[c] (%):					
Favored	97.73	94.16	97.32	96.07	95.97
Outliers	0.13	0.39	0	0.21	0.37

[a] Values in parentheses are for the highest-resolution shell.

[b] $CC_{1/2}$ correlation coefficient as defined in Karplus & Diederichs [74] and calculated by *XSCALE* [40].

[c] Calculated using the MolProbity server (http://molprobity.biochem.duke.edu) [75].

Table 2. Overview of EspG crystal structures.

Chaperone	PDB ID	Structure	Oligomerization	Species	Reference
$EspG_1$	5VBA		Monomer (dimerisation of T4L)	*M. kansasii*	This work
	4L4W		Wing-shaped dimer	*M. smegmatis*	This work
	4RCL		β8-mediated	*M. smegmatis*	This work
$EspG_3$	5SXL		Monomer	*M. smegmatis*	This work
	4W4J		Wing-shaped dimer	*M. smegmatis*	[27]
	4W4I		Monomer	*M. tuberculosis*	[27]
	5DLB		Monomer	*M. marinum*	This work
$EspG_5$	4KXR		Complex with PE25-PPE41	*M. tuberculosis*	[26]

$EspG_5$	4W4L		Complex with PE25-PPE41	*M. tuberculosis*	[27]
$EspG_5$	5XFS		Complex with PE8-PPE15	*M. tuberculosis*	[34]

Table 3. Collected SAXS data

Data collection parameters	
Instrument	P12 at EMBL/DESY, storage ring PETRA III, Germany
Beam geometry (mm^2)	0.2 × 0.12
Wavelength (Å)	1.24
q-range ($Å^{-1}$)	0.0023 – 0.47
Exposure time (ms)	20 × 50
Temperature (K)	283
Instrument	B21 at Diamond Light Source, United Kingdom
Beam geometry (mm^2)	1.0 x 5.0
Wavelength (Å)	1.0
q-range ($Å^{-1}$)	0.0038 – 0.42
Exposure time (ms)	60 x 100
Temperature (K)	283

Structural parameters

Sample	Conc. (mg ml^{-1})	$R_{g,\ Guinier}$ (nm)	$R_{g,\ Pr}$ (nm)	D_{max} (nm)	MM_{theor} (kDa)	MM_{SAXS} (kDa)	MM_{POROD} (kDa)	MM_{DAM} (kDa)	*Ab initio* Resolution, (Å)
$EspG_{1mma}$	1.0	2.7	2.9	9.7	29.8	25	43	45	42 ± 3
	2.0	3.2	3.1	11	29.8	32	55		
	4.2	3.4	3.5	11	29.8	37	65		
	6.0	3.5	3.6	12	29.8	40	72		
$EspG_{3mtb}$	1.1	2.5	2.6	9	31.6	23	41	41	34 ± 3

	2.0	2.8	3.0	10	31.6	30	47		
	4.0	3.2	3.1	10	31.6	32	56		
	6.1	3.5	3.5	12	31.6	39	68		
$EspG_{3mma}$	1.1	2.3	2.5	8	32.0	20	39	34	23 ± 2
	2.1	2.3	2.4	8	32.0	22	35	35	
	4.0	2.3	2.4	8	32.0	21	40	38	
	6.0	2.3	2.3	8	32.0	22	44	36	
$EspG_{3msm}$	0.78	2.5	2.6	8.56	31.6	20.54	39	48	36 ± 3
	1.75	2.5	2.5	8.83	31.6	21.37	32	41	
	3.94	2.6	2.6	9.25	31.6	22.06	39	44	
	6.24	2.8	2.7	9.71	31.6	23.97	39	47	
$EspG_{3msm}$ Se-Met	0.9	2.5	2.5	9.2	31.6	22.53	38		
	2.14	2.5	2.6	9.2	31.6	22.53	38		
	3.79	2.6	2.6	9.2	31.6	24.27	40	43	39 ± 3
$EspG_{5mtu}$	0.9	2.3	2.5	8	32.4	23	41	47	25± 2
	1.7	2.4	2.4	8	32.4	22	42		
	4.1	2.4	2.5	8	32.4	21	43		
	6.7	2.4	2.4	8	32.4	22	41		
PE25–PPE41–$EspG_{5mtu}$ complex	0.5	3.95	3.99	13.03	65	76	46	76	37 ± 3
PE5–PPE4–$EspG_{3mtu}$ complex	1.22	3.98	4.197	14.2	95	83	52	83	38 ± 3

Table 4a. Oligomer analysis using the crystallographic monomer and dimer structures of $EspG_{1mma}$.

Sample	Concentration (mg ml^{-1})	Monomeric fraction	Dimeric fraction	Goodness-of-the-Fit, chi^2
$EspG_{1mma}$	1.0	0.94	0.06	0.80
	2.0	0.74	0.26	0.93
	4.2	0.58	0.42	1.44
	6.0	0.50	0.50	1.90

Table 4b. Oligomer analysis using $EspG_{1mma}$ dimer structure based on template 4W4L $EspG_{3msm}$

Sample	Concentration (mg ml^{-1})	Monomeric fraction	Dimeric fraction	Goodness-of-the-Fit, chi^2
$EspG_{1mma}$	1.0	0.93	0.07	0.79
	2.0	0.72	0.28	0.86
	4.2	0.54	0.46	1.01
	6.0	0.43	0.57	1.27

Table 4c. Oligomer analysis of $EspG_{3mtu}$.

Sample	Concentration (mg ml^{-1})	Monomer fraction	Dimer fraction	Goodness-of-the-Fit, chi^2
$EspG_{3mtu}$	1.1	0.537	0.462	0.89
	2.0	0.364	0.636	0.90
	4.0	0.113	0.887	0.95
	6.1	0.0	0.999	0.89

Table 4d. Oligomer analysis of $EspG_{3mma}$.

Sample	Concentration (mg ml^{-1})	Monomer fraction	Dimer fraction	Goodness-of-the-Fit, chi^2
$EspG_{3mma}$	1.1	0.531	0.468	0.82
	2.1	0.195	0.805	0.88
	4.0	0.000	1.000	1.05
	6.0	0.00	1.000	1.69

Table 4e. Oligomer analysis of $EspG_{3msm}$.

Sample	Concentration (mg ml^{-1})	Monomer fraction	Dimer fraction	Goodness-of-the-Fit, chi^2
$EspG_{3msm}$	0.78	0.589	0.410	0.90
	1.75	0.654	0.346	1.32
	3.94	0.575	0.425	1.35
	6.24	0.449	0.550	2.03

References

[1] Pai M, Behr MA, Dowdy D, Dheda K, Divangahi M, Boehme CC, et al. Tuberculosis. Nat Rev Dis Primers. 2016;2:16076.

[2] Cole ST. Inhibiting Mycobacterium tuberculosis within and without. Philosophical transactions of the Royal Society of London Series B, Biological sciences. 2016;371.

[3] Stanley SA, Raghavan S, Hwang WW, Cox JS. Acute infection and macrophage subversion by *Mycobacterium tuberculosis* require a specialized secretion system. Proc Natl Acad Sci U S A. 2003;100:13001-6.

[4] Lewis KN, Liao R, Guinn KM, Hickey MJ, Smith S, Behr MA, et al. Deletion of RD1 from Mycobacterium tuberculosis mimics bacille Calmette-Guerin attenuation. J Infect Dis. 2003;187:117-23.

[5] Guinn KM, Hickey MJ, Mathur SK, Zakel KL, Grotzke JE, Lewinsohn DM, et al. Individual RD1-region genes are required for export of ESAT-6/CFP-10 and for virulence of *Mycobacterium tuberculosis*. Mol Microbiol. 2004;51:359-70.

[6] Houben EN, Korotkov KV, Bitter W. Take five - Type VII secretion systems of Mycobacteria. Biochim Biophys Acta. 2014;1843:1707-16.

[7] Groschel MI, Sayes F, Simeone R, Majlessi L, Brosch R. ESX secretion systems: mycobacterial evolution to counter host immunity. Nat Rev Microbiol. 2016;14:677-91.

[8] Houben EN, Bestebroer J, Ummels R, Wilson L, Piersma SR, Jimenez CR, et al. Composition of the type VII secretion system membrane complex. Mol Microbiol. 2012;86:472-84.

[9] Beckham KS, Ciccarelli L, Bunduc CM, Mertens HD, Ummels R, Lugmayr W, et al. Structure of the mycobacterial ESX-5 type VII secretion system membrane complex by single-particle analysis. Nat Microbiol. 2017;2:17047.

[10] van Winden VJ, Ummels R, Piersma SR, Jimenez CR, Korotkov KV, Bitter W, et al. Mycosins Are Required for the Stabilization of the ESX-1 and ESX-5 Type VII Secretion Membrane Complexes. mBio. 2016;7.

[11] Cole ST, Brosch R, Parkhill J, Garnier T, Churcher C, Harris D, et al. Deciphering the biology of *Mycobacterium tuberculosis* from the complete genome sequence. Nature. 1998;393:537-44.

[12] Abdallah AM, Gey van Pittius NC, Champion PA, Cox J, Luirink J, Vandenbroucke-Grauls CM, et al. Type VII secretion--mycobacteria show the way. Nat Rev Microbiol. 2007;5:883-91.

[13] Gey van Pittius NC, Sampson SL, Lee H, Kim Y, van Helden PD, Warren RM. Evolution and expansion of the *Mycobacterium tuberculosis* PE and PPE multigene families and their association with the duplication of the ESAT-6 (*esx*) gene cluster regions. BMC evolutionary biology. 2006;6:95.

[14] Strong M, Sawaya MR, Wang S, Phillips M, Cascio D, Eisenberg D. Toward the structural genomics of complexes: crystal structure of a PE/PPE protein complex from *Mycobacterium tuberculosis*. Proc Natl Acad Sci U S A. 2006;103:8060-5.

[15] Delogu G, Brennan MJ. Comparative immune response to PE and PE_PGRS antigens of Mycobacterium tuberculosis. Infect Immun. 2001;69:5606-11.

[16] Brennan MJ, Delogu G, Chen Y, Bardarov S, Kriakov J, Alavi M, et al. Evidence that mycobacterial PE_PGRS proteins are cell surface constituents that influence interactions with other cells. Infect Immun. 2001;69:7326-33.

[17] Banu S, Honore N, Saint-Joanis B, Philpott D, Prevost MC, Cole ST. Are the PE-PGRS proteins of Mycobacterium tuberculosis variable surface antigens? Mol Microbiol. 2002;44:9-19.

[18] Li Y, Miltner E, Wu M, Petrofsky M, Bermudez LE. A Mycobacterium avium PPE gene is associated with the ability of the bacterium to grow in macrophages and virulence in mice. Cellular microbiology. 2005;7:539-48.

[19] Sayes F, Sun L, Di Luca M, Simeone R, Degaiffier N, Fiette L, et al. Strong immunogenicity and cross-reactivity of Mycobacterium tuberculosis ESX-5 type VII secretion: encoded PE-PPE proteins predicts vaccine potential. Cell Host Microbe. 2012;11:352-63.

[20] Fortune SM, Jaeger A, Sarracino DA, Chase MR, Sassetti CM, Sherman DR, et al. Mutually dependent secretion of proteins required for mycobacterial virulence. Proc Natl Acad Sci U S A. 2005;102:10676-81.

[21] Sani M, Houben EN, Geurtsen J, Pierson J, de Punder K, van Zon M, et al. Direct visualization by cryo-EM of the mycobacterial capsular layer: a labile structure containing ESX-1-secreted proteins. PLoS Pathog. 2010;6:e1000794.

[22] Abdallah AM, Verboom T, Hannes F, Safi M, Strong M, Eisenberg D, et al. A specific secretion system mediates PPE41 transport in pathogenic mycobacteria. Mol Microbiol. 2006;62:667-79.

[23] Abdallah AM, Verboom T, Weerdenburg EM, Gey van Pittius NC, Mahasha PW, Jimenez C, et al. PPE and PE_PGRS proteins of *Mycobacterium marinum* are transported via the type VII secretion system ESX-5. Mol Microbiol. 2009;73:329-40.

[24] Bottai D, Di Luca M, Majlessi L, Frigui W, Simeone R, Sayes F, et al. Disruption of the ESX-5 system of *Mycobacterium tuberculosis* causes loss of PPE protein secretion, reduction of cell wall integrity and strong attenuation. Mol Microbiol. 2012;83:1195-209.

[25] Daleke MH, van der Woude AD, Parret AH, Ummels R, de Groot AM, Watson D, et al. Specific chaperones for the type VII protein secretion pathway. J Biol Chem. 2012;287:31939-47.

[26] Korotkova N, Freire D, Phan TH, Ummels R, Creekmore CC, Evans TJ, et al. Structure of the Mycobacterium tuberculosis type VII secretion system chaperone EspG5 in complex with PE25-PPE41 dimer. Mol Microbiol. 2014;94:367-82.

[27] Ekiert DC, Cox JS. Structure of a PE-PPE-EspG complex from Mycobacterium tuberculosis reveals molecular specificity of ESX protein secretion. Proc Natl Acad Sci U S A. 2014;111:14758-63.

[28] Daleke MH, Ummels R, Bawono P, Heringa J, Vandenbroucke-Grauls CM, Luirink J, et al. General secretion signal for the mycobacterial type VII secretion pathway. Proc Natl Acad Sci U S A. 2012;109:11342-7.

[29] Poulsen C, Panjikar S, Holton SJ, Wilmanns M, Song YH. WXG100 protein superfamily consists of three subfamilies and exhibits an alpha-helical C-terminal conserved residue pattern. PLoS One. 2014;9:e89313.

[30] Ramsdell TL, Huppert LA, Sysoeva TA, Fortune SM, Burton BM. Linked domain architectures allow for specialization of function in the FtsK/SpoIIIE ATPases of ESX secretion systems. J Mol Biol. 2015;427:1119-32.

[31] Rosenberg OS, Dovala D, Li X, Connolly L, Bendebury A, Finer-Moore J, et al. Substrates Control Multimerization and Activation of the Multi-Domain ATPase Motor of Type VII Secretion. Cell. 2015;161:501-12.

[32] Daleke MH, Cascioferro A, de Punder K, Ummels R, Abdallah AM, van der Wel N, et al. Conserved Pro-Glu (PE) and Pro-Pro-Glu (PPE) protein domains target LipY lipases of pathogenic mycobacteria to the cell surface via the ESX-5 pathway. J Biol Chem. 2011;286:19024-34.

[33] Phan TH, Ummels R, Bitter W, Houben EN. Identification of a substrate domain that determines system specificity in mycobacterial type VII secretion systems. Sci Rep. 2017;7:42704.

[34] Chen X, Cheng HF, Zhou J, Chan CY, Lau KF, Tsui SK, et al. Structural basis of the PE-PPE protein interaction in Mycobacterium tuberculosis. J Biol Chem. 2017;292:16880-90.

[35] Pierce BG, Wiehe K, Hwang H, Kim BH, Vreven T, Weng Z. ZDOCK server: interactive docking prediction of protein-protein complexes and symmetric multimers. Bioinformatics. 2014;30:1771-3.

[36] Biasini M, Bienert S, Waterhouse A, Arnold K, Studer G, Schmidt T, et al. SWISS-MODEL: modelling protein tertiary and quaternary structure using evolutionary information. Nucleic Acids Res. 2014;42:W252-8.

[37] Franke D, Jeffries CM, Svergun DI. Correlation Map, a goodness-of-fit test for one-dimensional X-ray scattering spectra. Nature methods. 2015;12:419-22.

[38] Matsumura M, Becktel WJ, Levitt M, Matthews BW. Stabilization of phage T4 lysozyme by engineered disulfide bonds. Proc Natl Acad Sci U S A. 1989;86:6562-6.

[39] Rosenbaum DM, Cherezov V, Hanson MA, Rasmussen SG, Thian FS, Kobilka TS, et al. GPCR engineering yields high-resolution structural insights into beta2-adrenergic receptor function. Science. 2007;318:1266-73.

[40] Kabsch W. Xds. Acta Crystallogr D Biol Crystallogr. 2010;66:125-32.

[41] McCoy AJ, Grosse-Kunstleve RW, Adams PD, Winn MD, Storoni LC, Read RJ. Phaser crystallographic software. J Appl Crystallogr. 2007;40:658-74.

[42] Zou Y, Weis WI, Kobilka BK. N-terminal T4 lysozyme fusion facilitates crystallization of a G protein coupled receptor. PLoS One. 2012;7:e46039.

[43] Cowtan K. Recent developments in classical density modification. Acta Crystallogr D Biol Crystallogr. 2010;66:470-8.

[44] Cowtan K. The Buccaneer software for automated model building. 1. Tracing protein chains. Acta Crystallogr D Biol Crystallogr. 2006;62:1002-11.

[45] Cowtan K. Fitting molecular fragments into electron density. Acta Crystallogr D Biol Crystallogr. 2008;64:83-9.

[46] Langer G, Cohen SX, Lamzin VS, Perrakis A. Automated macromolecular model building for X-ray crystallography using ARP/wARP version 7. Nat Protoc. 2008;3:1171-9.

[47] Emsley P, Lohkamp B, Scott WG, Cowtan K. Features and development of Coot. Acta Crystallogr D Biol Crystallogr. 2010;66:486-501.

[48] Afonine PV, Grosse-Kunstleve RW, Echols N, Headd JJ, Moriarty NW, Mustyakimov M, et al. Towards automated crystallographic structure refinement with phenix.refine. Acta Crystallogr D Biol Crystallogr. 2012;68:352-67.

[49] Arbing MA, Chan S, Harris L, Kuo E, Zhou TT, Ahn CJ, et al. Heterologous expression of mycobacterial Esx complexes in Escherichia coli for structural studies is facilitated by the use of maltose binding protein fusions. PLoS One. 2013;8:e81753.

[50] Gibson DG. Enzymatic assembly of overlapping DNA fragments. Methods Enzymol. 2011;498:349-61.

[51] Pape T, Schneider TR. HKL2MAP: a graphical user interface for phasing with SHELX programs. J Appl Cryst. 2004;37:843-4.

[52] Sheldrick GM. A short history of SHELX. Acta Crystallogr A. 2008;64:112-22.

[53] Sheldrick GM. Experimental phasing with SHELXC/D/E: combining chain tracing with density modification. Acta Crystallogr D Biol Crystallogr. 2010;66:479-85.

[54] Murshudov GN, Skubak P, Lebedev AA, Pannu NS, Steiner RA, Nicholls RA, et al. REFMAC5 for the refinement of macromolecular crystal structures. Acta Crystallogr D Biol Crystallogr. 2011;67:355-67.

[55] Vonrhein C, Blanc E, Roversi P, Bricogne G. Automated structure solution with autoSHARP. Methods Mol Biol. 2007;364:215-30.

[56] Adams PD, Afonine PV, Bunkoczi G, Chen VB, Davis IW, Echols N, et al. PHENIX: a comprehensive Python-based system for macromolecular structure solution. Acta Crystallogr D Biol Crystallogr. 2010;66:213-21.

[57] Painter J, Merritt EA. Optimal description of a protein structure in terms of multiple groups undergoing TLS motion. Acta Crystallogr D Biol Crystallogr. 2006;62:439-50.

[58] Painter J, Merritt EA. TLSMD web server for the generation of multi-group TLS models. J Appl Cryst. 2006;39:109-11.

[59] Blanchet CE, Spilotros A, Schwemmer F, Graewert MA, Kikhney A, Jeffries CM, et al. Versatile sample environments and automation for biological solution X-ray scattering experiments at the P12 beamline (PETRA III, DESY). J Appl Crystallogr. 2015;48:431-43.

[60] Guinier A. La diffraction des rayons X aux très petits angles : application à l'étude de phénomènes ultramicroscopiques. Ann Phys. 1939;11:161-237.

[61] Svergun DI. Determination of the regularization parameter in indirect-transform methods using perceptual criteria. J Appl Cryst. 1992;25:495-503.

[62] Petoukhov MV, Franke D, Shkumatov AV, Tria G, Kikhney AG, Gajda M, et al. New developments in the ATSAS program package for small-angle scattering data analysis. J Appl Crystallogr. 2012;45:342-50.

[63] Franke D, Svergun DI. DAMMIF, a program for rapid ab-initio shape determination in small-angle scattering. J Appl Crystallogr. 2009;42:342-6.

[64] Volkov VV, Svergun DI. Uniqueness of ab initio shape determination in small-angle scattering. J Appl Cryst. 2003;36:860-4.

[65] Tuukkanen AT, Kleywegt GJ, Svergun DI. Resolution of ab initio shapes determined from small-angle scattering. IUCrJ. 2016;3:440-7.

[66] Svergun D, Barberato C, Koch MHJ. CRYSOL - a program to pvaluate X-ray solution scattering of biological macromolecules from atomic coordinates. J Appl Cryst. 1995;28:768-73.

[67] Konarev PV, Volkov VV, Sokolova AV, Koch MHJ, Svergun DI. PRIMUS: a Windows PC-based system for small-angle scattering data analysis. J Appl Cryst. 2003;36:1277-82.

[68] Bernado P, Mylonas E, Petoukhov MV, Blackledge M, Svergun DI. Structural characterization of flexible proteins using small-angle X-ray scattering. J Am Chem Soc. 2007;129:5656-64.

[69] Tria G, Mertens HD, Kachala M, Svergun DI. Advanced ensemble modelling of flexible macromolecules using X-ray solution scattering. IUCrJ. 2015;2:207-17.

[70] Phillips JC, Braun R, Wang W, Gumbart J, Tajkhorshid E, Villa E, et al. Scalable molecular dynamics with NAMD. J Comput Chem. 2005;26:1781-802.

[71] MacKerell AD, Bashford D, Bellott M, Dunbrack RL, Evanseck JD, Field MJ, et al. All-atom empirical potential for molecular modeling and dynamics studies of proteins. J Phys Chem B. 1998;102:3586-616.

[72] Jorgensen WL, Chandrasekhar J, Madura JD, Impey RW, Klein ML. Comparison of simple potential functions for simulating liquid water. J Chem Phys. 1983;79:926-35.

[73] Humphrey W, Dalke A, Schulten K. VMD: visual molecular dynamics. J Mol Graph. 1996;14:33-8, 27-8.

[74] Karplus PA, Diederichs K. Linking crystallographic model and data quality. Science. 2012;336:1030-3.

[75] Chen VB, Arendall WB, 3rd, Headd JJ, Keedy DA, Immormino RM, Kapral GJ, et al. MolProbity: all-atom structure validation for macromolecular crystallography. Acta Crystallogr D Biol Crystallogr. 2010;66:12-21.